Journal of Physics B: Atomic, Molecular and Optical Physics

PAPER

Cross sections of K-shell ionization by electron impact, measured from threshold to 100 keV, for Au and Bi

To cite this article: J M Fernández-Varea *et al* 2014 *J. Phys. B: At. Mol. Opt. Phys.* **47** 155201

IOP Publishing Journal of Physics B: Atomic, Molecular and Optical Physics
J. Phys. B: At. Mol. Opt. Phys. **47** (2014) 155201 (9pp) doi:10.1088/0953-4075/47/15/155201

Cross sections of K-shell ionization by electron impact, measured from threshold to 100 keV, for Au and Bi

J M Fernández-Varea[1,2], V Jahnke[2], N L Maidana[2], A A Malafronte[2] and V R Vanin[2]

[1] Facultat de Física (ECM and ICC), Universitat de Barcelona, Diagonal 645, E-08028 Barcelona, Spain
[2] Instituto de Física, Universidade de São Paulo, Rua do Matão, Travessa R 187, Cidade Universitária, CEP: 05508-900 São Paulo, SP, Brazil

E-mail: jose@ecm.ub.edu

Received 2 April 2014, revised 5 June 2014
Accepted for publication 9 June 2014
Published 15 July 2014

Abstract

We have measured cross sections for the ionization of the K shell by electrons with energies from the respective thresholds up to 100 keV, for Au and Bi. The experimental values are obtained by dividing the number of counts in the Kα peak by the number of counts in an energy interval near the tip of the bremsstrahlung continuum, and multiplying this ratio by the theoretical estimate of bremsstrahlung emission towards the detector in this energy interval. Although such a procedure has already been described in the literature, here it is implemented avoiding some of the simplifications made in earlier works. Our experimental cross sections, which are the first ones to be reported for atoms with $Z > 47$ close to the threshold, are in reasonable agreement with the theoretical predictions of the semirelativistic distorted-wave Born approximation. Hippler's plane-wave Born approximation with corrections for Coulomb and exchange effects yields cross sections that are closer to the experimental data than those evaluated from the relativistic binary-encounter-Bethe model.

Keywords: atomic K shell, electron-impact ionization, distorted-wave Born approximation

(Some figures may appear in colour only in the online journal)

1. Introduction

The ionization of atoms by electron impact is a fundamental process of nature. It is therefore not surprising that the experimental and theoretical investigation of electron–atom ionizing collisions has occupied physicists for many decades, and that this topic is the subject of continued research. When the collision involves a tightly-bound shell the atom may emit, in the course of the subsequent relaxation process, a characteristic x-ray whose energy constitutes a fingerprint of the ionized shell and atom. This feature is exploited in a variety of applications, so that knowledge on accurate inner-shell ionization cross sections becomes an important issue. In spite of its long history, the theoretical study of inner-shell ionization by electrons (and other swift charged particles) is still challenging, and precision measurements are affected by difficulties that warrant further experimental work.

Liu and co-workers tabulated the experimental information available prior to year 2000 on measured K-shell ionization cross sections [1]. More measurements on atomic K shells have been carried out since then by the research group of Sichuan University [2–13], the collaboration between the Universities of Montpellier and Barcelona [14–17], as well as other authors [18–20]. Unfortunately, the results of [2–20] extend, at most, up to around 40 or 45 keV because the employed electron guns cannot be operated at higher energies. Hence, the methodologies set up in the aforementioned publications are constrained to measure K-shell ionization cross sections of atoms with atomic number $Z \lesssim 60$ (or x-ray production cross sections of L and higher shells). Moreover, from the compilation by Liu *et al* [1] and the very recent

comprehensive review by Llovet *et al* [21] it is apparent that there is a remarkable lack of experimental data for energies between 50 and 100 keV, precisely where the binding energies of atoms with $Z > 60$ are.

On the theoretical side, various *ab initio* formalisms have been proposed over the years to describe the ionization of inner shells in electron–atom collisions, such as the plane-wave [22, 23] and distorted-wave [24–26] Born approximations (PWBA and DWBA, respectively). The former approach describes the initial and final states of the projectile electron as plane waves, whereas the latter includes, in an approximate manner, the distortion caused by the atomic potential on the projectile's wave functions before and after the ionizing collision. In addition, the DWBA accounts for exchange effects in a consistent way, whereas the PWBA disregards them completely.

While *ab initio* methods like the DWBA demand quite intense numerical work, semiempirical approaches rely on a number of judicious simplifications that alleviate substantially the required computational effort. For instance, one may introduce approximate exchange and Coulomb corrections to the PWBA in order to improve its performance around the maximum of the ionization cross sections and even down to the threshold. Two semiempirical models that have received considerable attention are the one devised by Hippler [27–29], often abbreviated as PWBA-C-Ex, and the relativistic binary-encounter-Bethe (RBEB) model [30–32].

In the present article we report K-shell ionization cross sections by electron impact for Au ($Z = 79$) and Bi ($Z = 83$) measured between the corresponding threshold energies (80.7 and 90.5 keV, respectively) and 100 keV. In this near-threshold energy interval there are just a few measurements for Au, which display unexpectedly large discrepancies, and for Bi there is apparently not a single experimental value below 2 MeV. Besides providing new experimental ionization cross sections for the K shells of these atomic species, our data are also useful in the context of a more complete assessment of theoretical formalisms for $Z \gtrsim 60$. Recall that for the presently-considered energies and atomic numbers relativistic and exchange effects cannot be ignored and the distortion of the projectile's wave functions caused by the barely screened Coulomb potential of the nucleus is very strong. These features are a sensitive testing ground for the performance of theoretical frameworks. Although a deeper understanding of the collision dynamics can only be gained from experiments where fully differential cross sections are measured, many of these (e,2e) experiments yield relative distributions (see e.g. [33]), and then absolute total cross sections are needed to properly normalize such data. The reader is referred to the review article by Nakel and Whelan [34] for a thorough study of relativistic (e,2e) processes.

The rest of the article is organized as follows. Sections 2 and 3 describe in detail the experimental setup and data analysis procedures, respectively. The obtained results are presented in section 4, where they are compared to the existing experimental information and the prediction of theoretical and semiempirical formalisms. Finally, conclusions are drawn in section 5. The appendix summarizes simplified data analysis methods used by other researchers.

2. Experimental setup

Thin films of Au and Bi were irradiated with the continuous beam from the electron gun of the São Paulo Microtron Accelerator (Instituto de Física da Universidade de São Paulo, Brazil). The x-rays emitted by the excited atoms in the target were observed by means of a semiconductor detector. Since the K-shell ionization cross sections were deduced from the ratios between the number of Kα x-ray photons produced and the bremsstrahlung yield near the tip, it was essential to determine the detector response function in the neighbourhood of the full-energy peak besides its efficiency.

2.1. Electron beam

The 1.9 MeV continuous-wave injector of the São Paulo Microtron is currently operational and the 5 MeV recirculated booster is being commissioned. A brief description of this beam line can be found in [35]. In the present experiment, only the electrostatic electron gun was energized. The accelerating voltage was varied between 80 kV and 100 kV (the highest electrostatic potential that our electron gun can reach), with a ripple smaller than 0.3 kV as inferred from the electron bremsstrahlung spectra (*vide infra*). The beam was guided through the unpowered Microtron injector accelerating structures and deflected by a dipole magnet towards the vacuum chamber. The beam was then focused by a quadrupole triplet before the dipole magnet, and energy analysed by a C slit positioned just after the dipole; two additional quadrupoles provided the focus on the target. The electron current was selected to be between 150 and 250 nA so as to give appropriate photon counting rates.

2.2. Targets and vacuum chamber

Self-supporting samples were manufactured by the evaporation of metals Au or Bi on 10 μg cm^{-2}-thick graphite backings. The thicknesses of the deposited Au and Bi films were around 10 μg cm^{-2} and 8 μg cm^{-2}, respectively. The samples were mounted on 0.7 mm-thick C fiber frames and suspended by a light Al holder in the centre of the vacuum chamber. The choice of frame and holder materials contributed to the reduction of the background photon flux to negligible levels.

The vacuum chamber is made of stainless steel and its internal wall is lined with Al foil near the beam exit flange, which was framed with C to minimize unwanted electron bremsstrahlung. The beam was caught by a Faraday cup made of graphite, designed to reduce electron backscattering [36]. It was surrounded by Pb bricks (outside the vacuum chamber) to reduce the radiation background. A pneumatic arm positioned either the target or the view screen in the beam line, or left the beam track completely free to enable measurement of the electron current. The samples were positioned

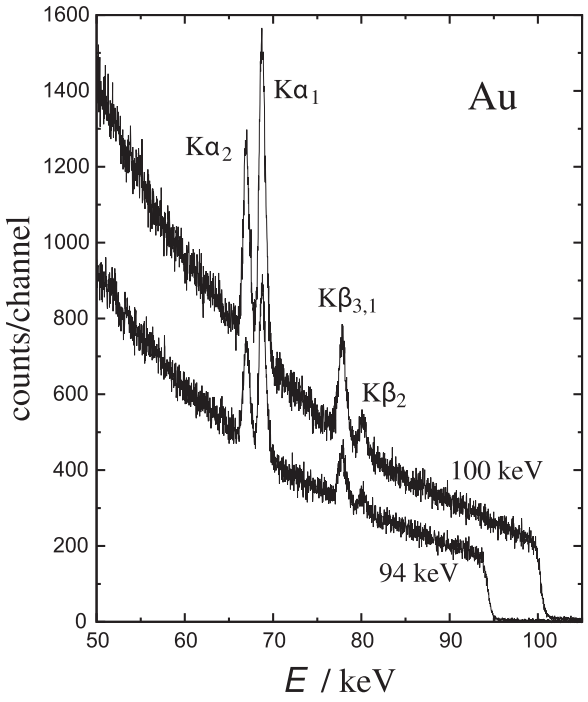

Figure 1. X-ray spectra of the Au/C sample as a function of photon energy. The displayed spectra pertain to the incidence of 94 and 100 keV electrons. The observed peaks (left to right) correspond to the Au $K\alpha_2$, $K\alpha_1$, $K\beta_{3,1}$ and $K\beta_2^{II,I}$ characteristic x-rays. The energy dispersion is 26 eV/channel.

perpendicular to the incident beam. The base pressure in the vacuum chamber was 3 mPa.

2.3. X-ray detection arrangement

A planar HPGe detector (ORTEC, 1000 series low energy photon spectrometer), 5 cm^2 in area and 1 cm thick, viewed the x-rays emitted from the target at $\theta = 120°$ with respect to the beam direction through a 50 μm-thick Al spectroscopy window. A Pb shield was internally lined with Cu all around the detector and the spectroscopy window, with the result that characteristic x-rays of Pb were not seen in the recorded spectra.

A spectroscopy amplifier with a 2 μs shaping time and pile-up rejection, and a 1.25 μs conversion time ADC (ORTEC NIM modules 572 and 927, respectively) were utilized to measure the spectra. The energy resolution (FWHM) was 790 eV at the 81 keV γ-ray of ^{133}Ba. Besides the ADC built-in livetime clock, a 60 Hz pulser was used to control the counting time. The dead time was kept below ~8% in all runs. However, the present results do not rely on the measurement time, as will be explained in section 3.1.

Simultaneously with the acquisition of the spectrum, the charge collected by the Faraday cup was integrated and stored in a scaler. Acquisition times varied between 20 and 80 min.

A couple of typical x-ray spectra are shown in figure 1. The Au $K\alpha_2$ and $K\alpha_1$ peaks are well resolved and the $K\beta_{3,1}$ doublet is also clearly visible on the continuous bremsstrahlung background. The statistics of the Au $K\beta_2^{II,I}$ doublet deteriorates rapidly as the beam energy approaches the K-shell ionization threshold.

2.4. Full-energy peak efficiency and response function of the detector

The full-energy peak efficiency curve $\varepsilon_{FE}(E)$ of the HPGe detector was determined having recourse to the γ- and x-rays emitted by activity-calibrated radioactive sources of ^{133}Ba, ^{137}Cs, ^{152}Eu, ^{207}Bi and ^{241}Am; the Pb x-rays from ^{207}Bi could be employed because the Cu lining of the detector shield prevented the stray fluorescence x-rays from the Pb shield reaching the detector.

The $\varepsilon_{FE}(E)$ curves of planar HPGe x-ray detectors usually show a plateau between around 30 and 70 keV [37], but in our case the efficiency rose ~10% above this plateau, up to energies approaching 80 keV. This artifact could be attributed to the development of a dead layer in the rim of the detector that did not extend to the central region [38] and, therefore, resulted in an overall good response to x- and γ-rays except for this bump in the full-energy peak efficiency curve. Anyway, to better characterize the behavior of $\varepsilon_{FE}(E)$, we added to the set of radioactive sources an activity-calibrated source of the short-lived radionuclide ^{198}Au which provided the efficiency for the Hg $K\alpha_1$ x-rays, i.e. very close to the Au K x-rays of interest.

The detector response function yields the average number of events at energy E for each photon of energy E' that enters the solid angle Ω subtended by the detector. It is suitably modelled by the convolution

$$R(E, E') = \varepsilon(E') \int dE''\, G(E'', s; E) \times [\delta(E'' - E') + P(E'', E')], \quad (1)$$

where the *intrinsic* efficiency $\varepsilon(E')$ of the detector is related to the full-energy peak efficiency through

$$\varepsilon_{FE}(E') = \frac{\Omega}{4\pi \text{ sr}}\, \varepsilon(E'). \quad (2)$$

$G(E'', s; E)$ stands for a normalized Gaussian function with average E'' and standard deviation s; the latter is represented by the usual function $s(E') = \sqrt{a + bE'}$ with parameters fitted to the full-energy peak FWHMs. δ is Dirac's delta function. Since $R(E, E')$ was needed only for energies greater than $E' - 5$ keV, a simple shape was adopted for the continuous component $P(E'', E')$ which includes a shelf and a shoulder to the left of the peak

$$P(E'', E') = \begin{cases} h & \text{if } E'' < E' - l, \\ h + m(E'' - E' + l) & \text{if } E' - l \leqslant E'' \leqslant E', \\ 0 & \text{if } E' < E''. \end{cases} \quad (3)$$

The parameters h, m and l were evaluated from the 59, 75, 81 and 121 keV peaks in the spectra of the calibration sources, and fitted with straight lines as a function of energy. Notice that, according to equation (1), $P(E'', E')$ must be normalized to one count in the full-energy peak. The detector resolution changed slightly with the actual conditions of each run, and

therefore the constant term a in $s(E')$ was reevaluated to reproduce the measured width of the Kα_1 peak of Au or Bi. This simple model and procedure was sufficient to ensure a good overall precision in the bremsstrahlung yield near the photon energy tip because the contribution of $P(E'', E')$ amounts to less than 5% of the observed spectra.

3. Data analysis

3.1. X-ray production cross sections

The primary quantity that can be extracted from the acquired photon spectra is, for a given peak associated to one or more atomic radiative transitions, the x-ray production cross section $\sigma^{\mathrm{x}}(E_{\mathrm{e}})$ at the various electron energies E_{e}. It is assumed that the electrons of the beam cross the target following a rectilinear trajectory. For an incidence angle α and a sample thickness d the path length is equal to $d/\cos\alpha$. Then, the number of characteristic x-rays of interest (energy E_{x}), N_{x}, is related to the number of impinging electrons, N_{e}, through

$$N_{\mathrm{x}} = \frac{C}{4\pi\ \mathrm{sr}}\,\sigma^{\mathrm{x}}(E_{\mathrm{e}})\,\varepsilon(E_{\mathrm{x}}) \tag{4}$$

with

$$C \equiv N_{\mathrm{e}}\,\mathcal{N}(d/\cos\alpha)\,\Omega, \tag{5}$$

where $\mathcal{N} = N_{\mathrm{A}}\rho/A_{\mathrm{w}}$ is the number of atoms per unit volume in the sample, being N_{A} the Avogadro constant, ρ the mass density and A_{w} the atomic weight.

From expressions (4) and (5) one can in principle isolate σ^{x} in terms of N_{e}, d, Ω and ε. However, sometimes the uncertainties associated with these quantities are too large. In the present experimental setup, the small solid angle of the Faraday cup precluded an accurate measurement of N_{e}, and we lacked a sufficiently precise independent estimate of d. In this context, it seemed preferable to adopt an alternative method to determine the x-ray emission cross section which would reduce the uncertainties to acceptable levels. A particularly expedient way to circumvent these experimental shortcomings takes advantage of the continuous bremsstrahlung component of the measured photon spectra, which is also proportional to the product $N_{\mathrm{e}}\mathcal{N}(d/\cos\alpha)\,\Omega$, equation (5). This analysis procedure, outlined in what follows, has been employed with success by various authors [39–44], albeit with some simplifications.

The relationship between the electron bremsstrahlung in the target and the observed number of counts in a given energy interval in the photon spectrum requires taking into account both the detector response function (as described in the preceding section) and the dispersion in energy of the electrons that emit braking radiation. The latter arises mainly from the fluctuations of the electrostatic potential in the electron gun and, to a lesser extent, from the randomness of the (very small) energy loss in the target. We consider that the electron energy distribution is well represented by a Gaussian function $G(E_{\mathrm{e}}, s_{\mathrm{e}}; E)$, where E_{e} is the average and s_{e} the root-mean-square deviation of the energy of the electrons that interact with the target.

As usual in this type of experiment, the detector employed to acquire the x-ray spectra has a small frontal area and is located far from the target, hence $\Omega \ll 4\pi$ sr and we can assume that the variation of bremsstrahlung intensity within this solid angle is negligible.

The number of counts in a specific energy interval (E_1, E_2) of the spectrum due to bremsstrahlung photons emitted by the film of the active element that impinge on the detector, N_{B}, is given by

$$N_{\mathrm{B}} = C\,I_{\mathrm{B}}(E_1, E_2) \tag{6}$$

with

$$I_{\mathrm{B}}(E_1, E_2) = \int_{E_1}^{E_2} \mathrm{d}E \int_0^{\infty} \mathrm{d}E'\,B(E_{\mathrm{e}}, s_{\mathrm{e}}; E')\,R(E, E') \tag{7}$$

which can be related to the doubly differential cross section (DDCS) $\mathrm{d}^2\sigma_{\mathrm{B}}/\mathrm{d}E\,\mathrm{d}\Omega$, for the emission of a bremsstrahlung photon with energy in the interval $(E, E + \mathrm{d}E)$ and initial direction in the solid angle $\mathrm{d}\Omega$ pointing towards the detector,

$$B(E_{\mathrm{e}}, s_{\mathrm{e}}; E') = \int_0^{\infty} \mathrm{d}E''\,\frac{\mathrm{d}^2\sigma_{\mathrm{B}}(E''; E', \theta)}{\mathrm{d}E\,\mathrm{d}\Omega}\,G(E_{\mathrm{e}}, s_{\mathrm{e}}; E''). \tag{8}$$

In practice, the integration domain in E'' is limited to a few s_{e} around the average electron energy E_{e}; thus, we define a maximum electron energy, $E_{\max}$, that corresponds to the channel in the photon energy spectrum where the bremsstrahlung continuum coalesces with the background, typically around 1 keV above E_{e}.

Dividing equation (4) by equation (6) we arrive at the final expression for the x-ray production cross section,

$$\sigma^{\mathrm{x}}(E_{\mathrm{e}}) = \frac{N_{\mathrm{x}}}{N_{\mathrm{B}}}\,\frac{4\pi\ \mathrm{sr}}{\epsilon(E_{\mathrm{x}})}\,I_{\mathrm{B}}(E_1, E_2), \tag{9}$$

which does not contain the (poorly-known) factor C. Simplified versions of this formula have been used hitherto in the data analysis of the measured x-ray spectra, see the Appendix.

The bremsstrahlung DDCS is customarily written as (see e.g. [45] and references therein)

$$\frac{\mathrm{d}^2\sigma_{\mathrm{B}}}{\mathrm{d}E\,\mathrm{d}\Omega} = \frac{Z^2}{\beta^2}\,\frac{1}{E}\,\chi(Z, E_{\mathrm{e}}, \kappa)\,S(Z, E_{\mathrm{e}}, \kappa;\ \cos\theta), \tag{10}$$

where β is the velocity of the electron divided by the speed of light in vacuum, $\chi(Z, E_{\mathrm{e}}, \kappa)$ is the total (i.e. electron-nucleus plus electron-electron) scaled bremsstrahlung DCS and $S(Z, E_{\mathrm{e}}, \kappa;\ \cos\theta)$ is the so-called shape function; $\kappa \equiv E/E_{\mathrm{e}}$ and θ is the photon emission polar angle. Seltzer and Berger [46] synthesized tables of $\chi(Z, E_{\mathrm{e}}, \kappa)$ which for $E_{\mathrm{e}} \leqslant 500$ keV rely on calculations carried out with partial-wave methods [47]. In turn, Kissel *et al* [48] performed partial-wave calculations to tabulate $S(Z, E_{\mathrm{e}}, \kappa;\ \cos\theta)$ for a very limited set of cases. These benchmark shape functions can be closely approximated by a simple analytical formula (the 'modified dipole' angular distribution) [45, 49].

3.2. Determination of N_x and N_B

The numbers of counts in the $K\alpha_{2,1}$ and $K\beta_{3,1}$ peaks of the K series were evaluated separately (transitions $KN_{2,3}$ have been disregarded owing to the small number of counts in the $K\beta_2^{II,I}$ peaks). In both cases a linear background was fitted in the neighbouring channels, and the area under this line in the channel region selected for each group of peaks was subtracted from the total number of counts in the spectrum. Since all chosen energy intervals were about 2 keV wide, the numbers of counts lost by the intrinsic atomic transition width were negligible.

The number of bremsstrahlung counts, N_B, along with the electron-beam parameters E_e and s_e needed in equation (9) to place the x-ray emission cross section on an absolute scale can be extracted from an energy interval (E_1, E_2) close to the tip of the bremsstrahlung spectrum. Specifically, E_e and s_e were obtained from a least-squares procedure [50] where the experimental spectrum in the interval $(E_e - 4\ \text{keV}, E_e + 1\ \text{keV})$ was fitted by expression (6). This choice avoided two important sources of error, one related to the detector response function far from the full-energy peak and the other linked to the photon background generated either by the electron beam hitting the Faraday cup or by electrons that scatter in the walls of the vacuum chamber and the target frame, which can be appreciable at low energies. However, the accurate description of the photon spectrum shape in the tip region demands a model for the energy distribution (dispersion) of the electron beam even if this involves a parameter otherwise irrelevant to this measurement, s_e in formula (8), because we have used thin targets and the ionization cross section varies smoothly with energy.

The net contribution of the Au or Bi active films to the bremsstrahlung spectrum in the interval (E_1, E_2) is $N_B = \sum'_i y_i^f$, where the prime indicates that the sum is restricted to channels that fulfill the condition $E_1 \leqslant E_i \leqslant E_2$ and $\{y_i^f\}$ is the raw spectrum $\{y_i\}$ after subtracting the contributions from pulse pileup, background, and bremsstrahlung that originates in the backing material. Pileup is important only in the tip region, and to evaluate it properly required correction for the natural background. To this end, we collected a spectrum $\{g_i\}$ of the natural background during a long time and defined the background-corrected spectrum as $y_i - r\ g_i$, where y_i is the number of counts in the ith channel of the raw spectrum and r is the ratio between the respective counting times. The pileup spectrum $\{p_i\}$ was then calculated as $p_i = \eta \sum_j y_{i-j}\ y_j$ with η evaluated to fit the number of counts in the p_i spectrum between $E_e + 5$ keV and $E_e + 50$ keV to the number of counts in the same region of the background-corrected spectrum, adopting a procedure similar to that proposed in [51]. In this energy interval, although pulse pileup dominates the raw spectrum, the natural background cannot be ignored. The uncertainty in p_i is mostly due to the number of counts in the interval used to normalize the pileup spectrum, which affects only η because the number of counts in the raw spectrum below E_e is much larger than above E_e. The variance of p_i is $\text{var}(p_i) = [\text{var}(\eta)/\eta^2]\, p_i^2$.

The net Au or Bi bremsstrahlung contribution in channel i is finally written as (Δ is the energy width of the channels)

$$y_i^f = y_i - p_i - r\ g_i - C_b\ I_{B,b}\left(E_i - \Delta/2, E_i + \Delta/2\right), \quad (11)$$

where $I_{B,b}$ is the bremsstrahlung integral for the backing material, i.e. equations (7) and (8) with the DDCS belonging to the atoms of the backing. The factor $C_b = N_e\, \mathcal{N}_b (d_b/\cos\alpha)\, \Omega$ is calculated with the measured values of N_e, Ω and $\mathcal{N}_b d_b$; the latter is the number of atoms per unit area of the backing. The backing contributes about 2% to the bremsstrahlung spectrum so that the comparatively large uncertainty of C_b barely increases the uncertainty of the final result.

The least-squares procedure consisted of minimizing the merit function

$$Q\left(C; E_e, s_e\right) = \sum_i{}' \frac{\left[y_i^f - C\ I_B\left(E_i - \frac{\Delta}{2}, E_i + \frac{\Delta}{2}\right)\right]^2}{\text{var}\left(y_i^f\right)} \quad (12)$$

with $\text{var}(y_i^f) = y_i + [\text{var}(\eta)/\eta^2]\, p_i^2 + r^2 g_i$, neglecting for the fit the uncertainty in the bremsstrahlung emitted by the backing, which affects all channels in a systematic way rather than randomly. However, the uncertainty in the total number of counts from the backing was propagated to the cross-section standard deviation.

Notice that the model function for y_i^f, $C\ I_B$, is linear in C and nonlinear in the variables E_e and s_e embodied in I_B. As a consequence, for a given pair of values E_e and s_e the quantity C' that minimizes Q can be calculated easily. The bidimensional function $Q(C'; E_e, s_e)$ is then minimized straightforwardly; $\hat{E}_e$ and $\hat{s}_e$ denote the values that minimize Q, and $\hat{C} = C'(\hat{E}_e, \hat{s}_e)$. Since the number of counts is $\sim 10^2 - 10^3$ in most of the channels in the (E_1, E_2) interval, and ~ 1 in just a few channels near E_2, the minimum value of Q is very approximately distributed like a χ^2 random variable. Therefore, Q can be used to assess the goodness of the fit. Figure 2 plots level curves of Q near its minimum value $Q(\hat{C}; \hat{E}_e, \hat{s}_e)$. The ellipsoidal shape of the curves hints at a good fit, which is confirmed by the comparison between the experimental and fitted spectra shown in figure 3. Another sign of consistency of the described procedure is that the $\hat{C}/N_e$ ratios resulting from the spectra generated when the same sample is irradiated with various beam energies are compatible within statistical uncertainties.

3.3. Ionization cross sections

After a vacancy has been created in the K shell, the excited atom relaxes to the ground state via the emission of various types of fluorescent radiation. The relationship between the K-shell ionization cross section σ_K and the production cross section of $K\alpha_{2,1}$ x-rays is

$$\sigma^x_{K\alpha_{2,1}} = \frac{\Gamma_{KL_{2,3}}}{\Gamma_{K,\text{total}}}\, \omega_K\, \sigma_K; \quad (13)$$

similar expressions hold for other dipole-allowed transitions

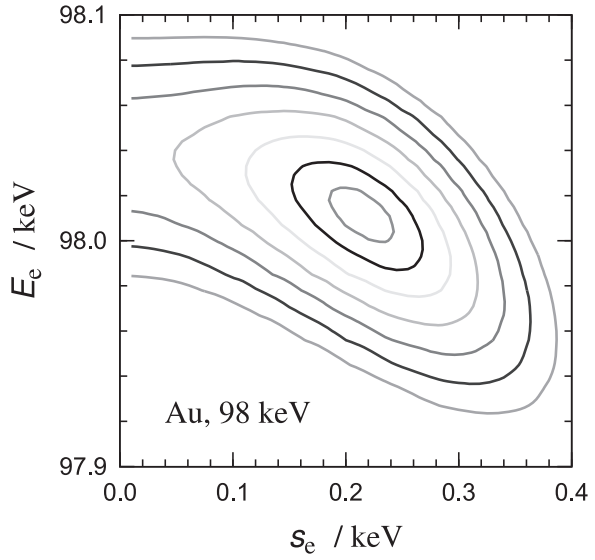

Figure 2. Level curves of the merit function $Q\left(C'; E_e, s_e\right)$ as a function of E_e and s_e for the 98 keV beam impinging on the Au/C sample. As explained in the text, C' is the value that minimizes Q for the given coordinates. The displayed level curves correspond to $Q\left(\hat{C}; \hat{E}_e, \hat{s}_e\right) + n^2$ with $n = 1, 2, \ldots, 7$.

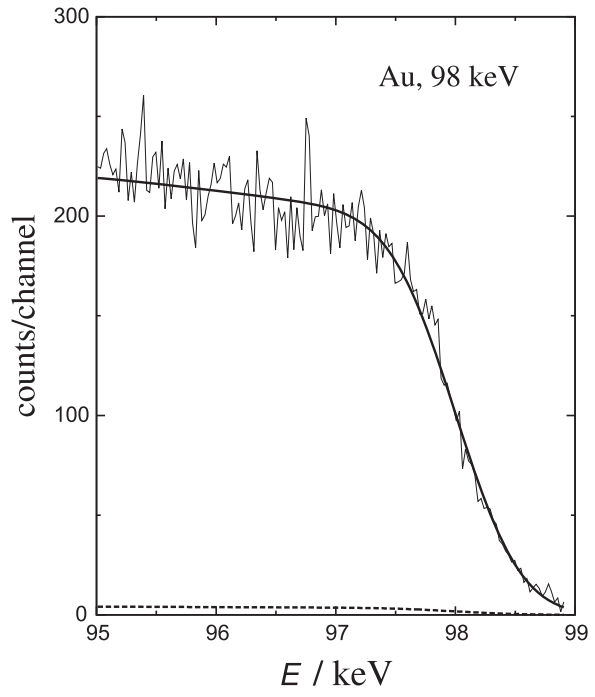

Figure 3. Experimental spectrum of the 98 keV beam impinging on the Au/C sample (dots joined by lines). The continuous curve is the spectrum calculated with formula (6) using the fitted values of $\hat{C}$, $\hat{E}_e$ and $\hat{s}_e$, added to the contribution of the C backing (dashed curve). The energy dispersion is 26 eV/channel.

belonging to the K series. Here, ω_K is the fluorescence yield and $\Gamma_{KX}/\Gamma_{K,total}$ is the ratio of x-ray emission rates. The adopted atomic relaxation parameters, taken from the classical compilations of Krause [52] (fluorescence yields) and Scofield [53] (emission rates) are given in table 1.

Table 1. Fluorescence yields [52] and ratios of x-ray emission rates [53] of Au and Bi.

Element	Z	ω_K	$\Gamma_{KL_{2,3}}/\Gamma_{K,total}$
Au	79	0.964	0.790
Bi	83	0.968	0.786

Table 2. Main sources of uncertainties in the cross sections of Au and Bi. The values quoted in the second column are estimates of the relative standard deviations in the cross section due to the quantities in the first column.

Contributor	Uncertainty (%)
Kα counts, N_x	1.5–17
Bremsstrahlung counts, N_B	<1
Relative intrinsic efficiency, $\varepsilon(E)/\varepsilon\left(E_x\right)$	<1
Measurement angle, θ	6
Bremsstrahlung DDCS, $d^2\sigma_B/dE\, d\Omega$	10
Relaxation data, ω_K and $\Gamma_{KL_{2,3}}/\Gamma_{K,total}$	<1

For the determination of σ_K we have employed the peaks pertaining to the $KL_{2,3}$ and the group formed by all other K transitions. Since both groups of transitions gave consistent results in all but for the near-threshold runs, where the Kβ transitions did not stand out from the continuous part of the spectrum, and the precision of the result obtained from the Kβ peaks is much lower than that obtained with the $KL_{2,3}$ transitions, the quoted results were obtained only with the latter transitions.

3.4. Uncertainty budget

Table 2 summarizes the main sources of uncertainty in the obtained cross section values. The Kα counting statistics varies from one of the unimportant contributions to the dominating one as the electron energy decreases from 100 keV to the K-shell ionization threshold and, along with the bremsstrahlung yield counting, give statistical uncertaintities that affect differently the results at different energies. The remaining sources of uncertainty have a systematic character.

The uncertainty in the bremsstrahlung DDCS was taken from [47], which states that the accuracy of the tabulated theoretical DDCSs is 10%. Another aspect of uncertainty related to the bremsstrahlung DDCS comes from the angle at which the detector is positioned, which has an uncertainty of about 2° in the reaction plane; the variation of the bremsstrahlung DDCS in this angular interval yields the relative uncertainty quoted in table 2.

An interesting property of the relative method for the measurement of cross sections is that the film thickness d does not appear in equation (9), and d is therefore also absent from the uncertainty budget. For the same reason, the uniformity of the mass distribution in the film is not important when

Table 3. Present K-shell ionization cross sections of Au and Bi by electron impact. The uncertainties in electron energies E_e are 0.03 keV whereas those in σ_K are given in parentheses, in units of the quantities' last digit, and correspond to one standard deviation. Notice that the uncertainties in σ_K include only the first two contributions listed in table 2.

Au		Bi	
E_e /keV	σ_K /b	E_e /keV	σ_K /b
82.91	0.36(4)	92.01	0.17(3)
84.41	0.76(2)	93.91	0.49(3)
86.63	1.16(3)	95.79	0.72(3)
88.05	1.39(4)	98.08	0.98(4)
90.38	1.81(4)	99.86	1.26(4)
91.91	2.04(4)		
94.31	2.37(5)		
96.01	2.54(5)		
98.01	2.83(5)		
100.26	3.11(5)		

dimensions of the order of the beam spot size (2 mm in diameter) are considered. Anyway, for each irradiation we estimated the average number of atoms per unit area of the active element in the part of the film hit by the electron beam, $\mathcal{N}d$, inserting in equations (5) and (6) the measured values of N_B (corrected for live counting time), N_e and Ω. The values of $\mathcal{N}d$ deduced in this way from the irradiations at all energies formed normal datasets with relative standard deviations of 12% (Au) and 9% (Bi), well within the expected uncertainties of the factors entering equation (5). This suggests that the active element is distributed rather uniformly because the electron beam did not hit exactly the same portion of the sample in all runs.

4. Results and discussion

The measured K-shell ionization cross sections of Au and Bi by electron bombardment are listed in table 3, where only the statistical uncertainties are quoted, and shown in figures 4 and 5 with uncertainty bars evaluated by combining in quadrature the statistical and systematic standard deviations (see table 2). The present experimental values, which extend from the corresponding ionization thresholds up to 100 keV, are depicted as circles. Other symbols indicate experimental data taken from the literature, when available. Both figures include the predictions of the semirelativistic DWBA as continuous curves. These theoretical cross sections, calculated by Bote and Salvat [26], were actually borrowed from the database incorporated in the PENELOPE Monte Carlo code system [49] instead of the parameterization of [56] so as to avoid possible errors that could be introduced by that analytical fit close to the thresholds. Finally, cross sections computed with the semiempirical PWBA-C-Ex and RBEB approaches are displayed as dashed and dot-dashed curves, respectively. Hippler's PWBA-C-Ex model [27–29] merely requires a

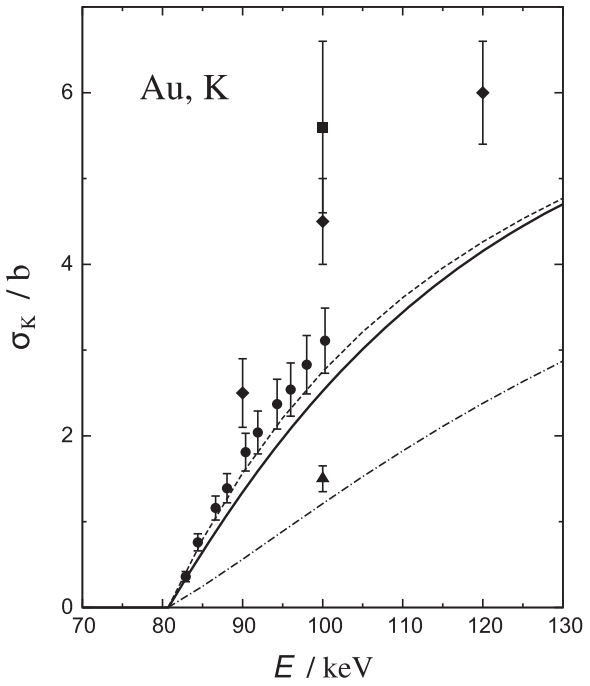

Figure 4. K-shell ionization cross section of Au as a function of energy. The present results are plotted as circles; the uncertainty bars include all the contributions listed in table 2. Other symbols are experimental data from [54] (■), [55] (♦) and [42] (▲). The continuous curve indicates the DWBA. The dashed and dot-dashed curves correspond, respectively, to the semiempirical PWBA-C-Ex and RBEB models.

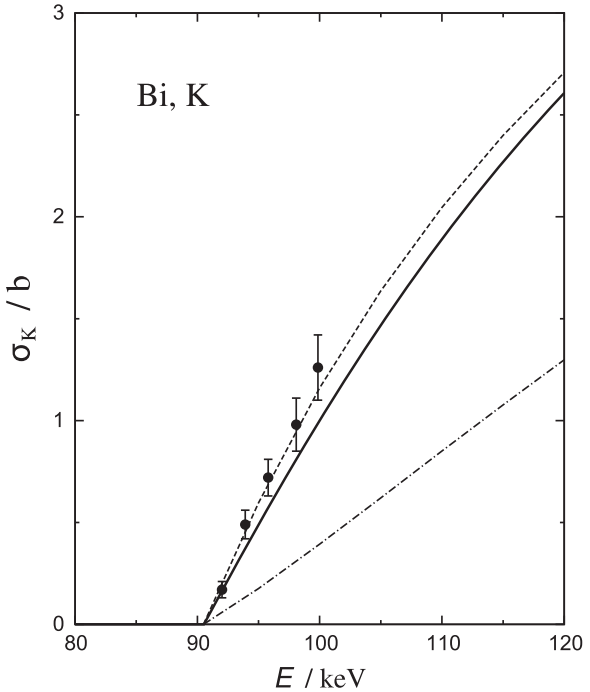

Figure 5. K-shell ionization cross section of Bi as a function of energy. The present results are plotted as circles; the uncertainty bars include all the contributions listed in table 2. The continuous curve indicates the DWBA. The dashed and dot-dashed curves correspond, respectively, to the semiempirical PWBA-C-Ex and RBEB models.

double numerical integral of the doubly differential ionization cross section, which is proportional to the generalizad oscillator strength of the active orbital, over energy and momentum transfers. In turn, the RBEB model of Kim and coworkers [30–32] makes additional simplifications which render an analytical expression that is straightforward to evaluate.

In the case of Au, we have the older measurements done by Motz and Placious [54], Davis *et al* [55] and Westbrook and Quarles [42]. These results are seen to be clearly discrepant. For instance, at 100 keV the cross sections reported by these authors differ by almost a factor of 4. There is reasonable agreement between our measured cross sections and the predictions of the DWBA. Hippler's model performs rather well, with cross sections that are only a few percent above the DWBA calculations. This is surprising because the PWBA-C-Ex is based on a non-relativistic hydrogenic generalized oscillator strength, which is *a priori* not expected to represent faithfully the response of an electron in the $1s_{1/2}$ orbital of a heavy atom to the perturbation of the passing projectile. On the other hand, the RBEB cross sections depart visibly from the trend of the experimental values, the DWBA and Hippler's PWBA-C-Ex model.

To our knowledge, there are no experimental values for the K shell of Bi below 2 MeV [1, 21]. As in the case of Au, our measurements are slightly above the DWBA cross sections and very close to Hippler's corrected PWBA.

5. Conclusions

We have measured the cross section for the ionization of the K shell of Au and Bi by electrons with energy between the respective thresholds and 100 keV. Our experimental values are in reasonable agreement with calculations carried out within the framework of the DWBA.

Finally, we would like to stress that a more complete knowledge of K-shell ionization cross sections of heavy atoms close to the threshold might be helpful in developing improved theoretical approaches.

Acknowledgments

We thank MSc W G P Engel for preparing the samples, and Professor M N Martins and the technical staff of the São Paulo Microtron for their valuable help in the operation of the accelerator. We are also indebted to Dr X Llovet for clarifying discussions. This work was performed with funding from the Brazilian agencies FAPESP (Fundação de Amparo à Pesquisa do Estado de São Paulo) and CNPq (Conselho Nacional de Desenvolvimento Científico e Tecnológico). J M Fernández-Varea is also grateful for the financial support from the Brazilian Coordenação de Aperfeiçoamento de Pessoal de Nível Superior (program CAPES-PVE) as well as the Spanish Ministerio de Ciencia e Innovación (project no. FPA2009-14091-C02-01) and FEDER.

Appendix. Simplified analysis methods

Our analysis procedure estimates the x-ray production cross section from the measured ratio N_x/N_B and theoretical bremsstrahlung DDCSs, see equation (9). In this appendix we briefly describe simplifications thereof that have been employed by other researchers.

The bremsstrahlung integral $I_B\left(E_1, E_2\right)$ that appears in the expression for N_B, equation (6), can be simplified to a more manageable form in the following way. Firstly, one may disregard the energy dispersion of the electron beam by replacing $G\left(E_e, s_e; E''\right)$ in equation (8) with $\delta\left(E'' - E_e\right)$. Secondly, the crude model $R\left(E, E'\right) = \varepsilon\left(E'\right)\delta\left(E - E'\right)$ for the response function of the detector may be inserted in equation (7) [in equation (1) make $P = 0$ and collapse the Gaussian to a Dirac delta function]. We get

$$N_B = C \int_{E_1}^{E_2} \mathrm{d}E\ \varepsilon\left(E\right) \frac{\mathrm{d}^2\sigma_B}{\mathrm{d}E\ \mathrm{d}\Omega} \tag{A.1}$$

with C defined in equation (5). Dividing equation (4) by equation (A.1) we arrive at the following expression for the absolute x-ray production cross section

$$\sigma^x\left(E_e\right) = \frac{N_x}{N_B} \frac{4\pi\ \mathrm{sr}}{\varepsilon\left(E_x\right)} \int_{E_1}^{E_2} \mathrm{d}E\ \varepsilon\left(E\right) \frac{\mathrm{d}^2\sigma_B}{\mathrm{d}E\ \mathrm{d}\Omega}. \tag{A.2}$$

Notice the dependence of σ^x on the relative intrinsic efficiency $\varepsilon\left(E\right)/\varepsilon\left(E_x\right)$.

Westbrook and Quarles [42] as well as Schneider *et al* [43] took the energy interval $\left(E_1, E_2\right)$ just beneath the characteristic x-ray peak of interest. Then $\varepsilon\left(E\right) = \varepsilon\left(E_x\right)$ and equation (A.2) reduces to

$$\sigma^x\left(E_e\right) = \frac{N_x}{N_B} 4\pi\ \mathrm{sr} \int_{E_1}^{E_2} \mathrm{d}E\ \frac{\mathrm{d}^2\sigma_B}{\mathrm{d}E\ \mathrm{d}\Omega}. \tag{A.3}$$

Schneider *et al* [43] made yet another simplification, neglecting the variation of the DDCS with energy if $\Delta E \equiv E_2 - E_1$ is small enough, which leads to

$$\sigma^x\left(E_e\right) = \frac{N_x}{N_B} 4\pi\ \mathrm{sr}\ \frac{\mathrm{d}^2\sigma_B}{\mathrm{d}E\ \mathrm{d}\Omega}\ \Delta E. \tag{A.4}$$

References

[1] Liu M, An Z, Tang C, Luo Z, Peng X and Long X 2000 *At. Data Nucl. Data Tables* **76** 213
[2] An Z, Tang C H, Zhou C G and Luo Z M 2000 *J. Phys. B: At. Mol. Opt. Phys.* **33** 3677
[3] Zhou C, Fu Y, An Z, Tang C and Luo Z 2001 *Chin. Phys. Lett.* **18** 531
[4] Zhou C, An Z and Luo Z 2001 *Chin. Phys. Lett.* **18** 759
[5] Luo Z, Tang C, An Z, He F, Peng X and Long X 2001 *Phys. Rev.* A **63** 034702
[6] Zhou C, Luo Z, Tang C and An Z 2001 *Radiat. Phys. Chem.* **61** 585
[7] Zhou C, An Z and Luo Z 2002 *J. Phys. B: At. Mol. Opt. Phys.* **35** 841

[8] Tang C, An Z, Luo Z and Liu M 2002 *J. Appl. Phys.* **91** 6739
[9] An Z, Liu M T, Fu Y C, Luo Z M, Tang C H, Li C M, Zhang B H and Tang Y J 2003 *Nucl. Instrum. Methods* B **207** 268
[10] Zhu J, An Z, Liu M and Tian L 2009 *Phys. Rev.* A **79** 052710
[11] Wu Y, An Z, Duan Y M and Liu M T 2010 *Nucl. Instrum. Methods* B **268** 2820
[12] Wu Y, An Z, Duan Y M, Liu M T and Wu J 2011 *Nucl. Instrum. Methods* B **269** 117
[13] Wu Y, An Z, Duan Y M, Liu M T and Ouyang X P 2012 *Can. J. Phys.* **90** 125
[14] Llovet X, Merlet C and Salvat F 2000 *J. Phys. B: At. Mol. Opt. Phys.* **33** 3761
[15] Llovet X, Merlet C and Salvat F 2002 *J. Phys. B: At. Mol. Opt. Phys.* **35** 973
[16] Merlet C, Llovet X and Salvat F 2004 *Phys. Rev.* A **69** 032708
[17] Merlet C, Llovet X and Fernández-Varea J M 2006 *Phys. Rev.* A **73** 062719
Merlet C, Llovet X and Fernández-Varea J M 2006 *Phys. Rev.* A **74** 049901 (erratum)
[18] Rejoub R, Lindsay B G and Stebbings R F 2002 *Phys. Rev.* A **65** 042713
[19] Singh R K and Shanker R 2003 *J. Phys. B: At. Mol. Opt. Phys.* **36** 3031
[20] Limandri S P, Vasconcellos M A Z, Hinrichs R and Trincavelli J C 2012 *Phys. Rev.* A **86** 042701
[21] Llovet X, Powell C J, Salvat F and Jablonski A 2014 *J. Phys. Chem. Ref. Data* **43** 013102
[22] Inokuti M 1971 *Rev. Mod. Phys.* **43** 297
[23] Madison D H and Merzbacher E 1975 *Atomic Inner-Shell Processes* ed B Crasemann (New York: Academic Press) pp 1–69
[24] Segui S, Dingfelder M and Salvat F 2003 *Phys. Rev.* A **67** 062710
[25] Colgan J, Fontes C J and Zhang H L 2006 *Phys. Rev.* A **73** 062711
[26] Bote D and Salvat F 2008 *Phys. Rev.* A **77** 042701
[27] Hippler R 1990 *Phys. Lett.* A **144** 81
[28] Khare S P and Wadehra J M 1996 *Can. J. Phys.* **74** 376
[29] An Z, Luo Z M and Tang C 2001 *Nucl. Instrum. Methods* B **179** 334
[30] Kim Y-K, Santos J P and Parente F 2000 *Phys. Rev.* A **62** 052710
[31] Santos J P, Parente F and Kim Y-K 2003 *J. Phys. B: At. Mol. Opt. Phys.* **36** 4211
[32] Guerra M, Parente F, Indelicato P and Santos J P 2012 *Int. J. Mass Spectrom.* **313** 1
[33] Sauter M, Keller N and Nakel W 1998 *J. Phys. B: At. Mol. Opt. Phys.* **31** L947
[34] Nakel W and Whelan C T 1999 *Phys. Rep.* **315** 409
[35] Vanin V R *et al* 2011 *AIP Conf. Proc.* **1351** 105
[36] Pino N L 2011 *Bremsstrahlung de Elétrons no Microtron do IFUSP: Medidas, Simulação e Proposta de Aplicação ao Estudo da Ressonancia Fluorescente Nuclear* (Brazil: Universidade de São Paulo) www.teses.usp.br/
[37] Knoll G F 2000 *Radiation Detection and Measurement* 3rd edn (Hoboken, NJ: Wiley)
[38] Maidana N L, Vanin V R, Jahnke V, Fernández-Varea J M, Martins M N and Brualla L 2013 *Nucl. Instrum. Methods* A **729** 371
[39] Hippler R, McGregor I, Aydinol M and Kleinpoppen H 1981 *Phys. Rev.* A **23** 1730
[40] Quarles C and Semaan M 1982 *Phys. Rev.* A **26** 3147
[41] Quarles C A and Estep L 1986 *Phys. Rev.* A **34** 2488
[42] Westbrook G L and Quarles C A 1987 *Nucl. Instrum. Methods* B **24/25** 196
[43] Schneider H, Tobehn I, Ebel F and Hippler R 1993 *Phys. Rev. Lett.* **71** 2707
[44] Campos C S, Vasconcellos M A Z, Llovet X and Salvat F 2002 *Phys. Rev.* A **66** 012719
[45] Salvat F, Fernández-Varea J M, Sempau J and Llovet X 2006 *Radiat. Phys. Chem.* **75** 1201
[46] Seltzer S M and Berger M J 1986 *At. Data Nucl. Data Tables* **35** 345
[47] Pratt R H, Tseng H K, Lee C M and Kissel L 1977 *At. Data Nucl. Data Tables* **20** 175
Pratt R H, Tseng H K, Lee C M and Kissel L 1981 *At. Data Nucl. Data Tables* **26** 477 (erratum)
[48] Kissel L, Quarles C A and Pratt R H 1983 *At. Data Nucl. Data Tables* **28** 381
[49] Salvat F, Fernández-Varea J M and Sempau J 2011 *PENELOPE-2011: A Code System for Monte Carlo Simulation of Electron and Photon Transport* (Issy-les-Moulineaux: OECD/NEA)
[50] Eadie W T, Drijard D, James F E, Roos M and Sadoulet B 1971 *Statistical Methods in Experimental Physics* (Amsterdam: North-Holland)
[51] do Nascimento E, Fernández-Varea J M, Vanin V R and Maidana N L 2011 *AIP Conf. Proc.* **1351** 216
[52] Krause M O 1979 *J. Phys. Chem. Ref. Data* **8** 307
[53] Scofield J H 1974 *At. Data Nucl. Data Tables* **14** 121
[54] Motz J W and Placious R C 1964 *Phys. Rev.* **136** A662
[55] Davis D V, Mistry V D and Quarles C A 1972 *Phys. Lett* **38A** 169
[56] Bote D, Salvat F, Jablonski A and Powell C J 2009 *At. Data Nucl. Data Tables* **95** 871
Bote D, Salvat F, Jablonski A and Powell C J 2011 *At. Data Nucl. Data Tables* **97** 186 (erratum)